



RESEARCH ARTICLE

10.1029/2018GC008090

Key Points:

- Fast *SV* velocity anomalies are observed in the upper part of the transition zone near subducted slabs in the western Pacific
- The observed anomalies are compatible with anisotropy due to lattice-preferred orientation in wadsleyite
- The fast *SV* velocity anomalies may imply a low water content, notably beneath the Tonga-Kermadec, the Philippines, and the Sumatra trenches

Supporting Information:

- Supporting Information S1

Correspondence to:

S.-J. Chang,
sjchang@kangwon.ac.kr

Citation:

Chang, S.-J., & Ferreira, A. M. G. (2019). Inference on water content in the mantle transition zone near subducted slabs from anisotropy tomography. *Geochemistry, Geophysics, Geosystems*, 20, 1189–1201. <https://doi.org/10.1029/2018GC008090>

Received 16 NOV 2018

Accepted 18 JAN 2019

Accepted article online 13 FEB 2019

Published online 27 FEB 2019

©2019. The Authors.

This is an open access article under the terms of the Creative Commons Attribution License, which permits use, distribution and reproduction in any medium, provided the original work is properly cited.

Inference on Water Content in the Mantle Transition Zone Near Subducted Slabs From Anisotropy Tomography

Sung-Joon Chang¹ and Ana M. G. Ferreira^{2,3}

¹Division of Geology and Geophysics, Kangwon National University, Chuncheon, South Korea, ²CERIS, Instituto Superior Tecnico, Universidade de Lisboa, Lisbon, Portugal, ³Department of Earth Sciences, University College London, London, UK

Abstract We examine the patterns of radial anisotropy in global tomography images of the mantle transition zone near subducted slabs in the western Pacific. Fast *SV* velocity anomalies are observed in this region, which are compatible with anisotropy due to lattice-preferred orientation in wadsleyite. Using mineral physics reports of the dependency of the strength of radial anisotropy on water content in wadsleyite, we estimate the water content in the transition zone near subducted slabs from the tomography images. We find that fast *SV* anisotropy anomalies over ~1.5% observed beneath subduction zones in the western Pacific are compatible with a low water content (smaller than ~3,000 ppm H/SI), notably beneath the Tonga-Kermadec trenches, the Philippines, and the Sumatra trench.

Plain Language Summary Tectonic plates plunge into the mantle at trenches, carrying water from the oceans. Some of this water may go down to the mantle transition zone between 410- and 660-km depth, where minerals have a large water storage capacity. In this study, we use observations of seismic anisotropy, the directional dependency of seismic wave speed, which is sensitive to the water content in the mantle transition zone. We find that the mantle transition zone beneath some subduction zones is drier than previously thought.

1. Introduction

The mantle transition zone (MTZ) has been suggested to play a key role in the mixing between the upper and lower mantle and in the cycling of fluids and volatiles in the Earth's deep interior (e.g., Hirschmann, 2006). The dominant mineral phases in this region, wadsleyite and ringwoodite, have a great capacity to store water up to 3 wt. % (e.g., Kohlstedt et al., 1996; Smyth, 1987), making the MTZ a potential water reservoir (e.g., Bercovici & Karato, 2003). On the other hand, many subducting slabs stagnate in the MTZ (e.g., Fukao & Obayashi, 2013), which suggests that the MTZ is a boundary layer in mantle convection. Therefore, it is crucial to understand the properties of the MTZ in order to constrain mantle convection and evolution.

Seismic anisotropy has been observed in both the uppermost and lowermost mantle (e.g., Nowacki et al., 2011; Silver, 1996), which is compatible with the idea that strong anisotropy should develop at boundary layers in the mantle (Montagner, 1998). When interpreted together with information from mineral physics, radial anisotropy can in particular provide information on vertical versus horizontal mantle flow by linking the seismic observations to anisotropy due to the lattice-preferred orientation (LPO) of mantle minerals (e.g., Chang et al., 2014; Montagner, 1998). In addition, shape-preferred orientation (SPO) due to the alignment of cracks, melts or alternating layers with large velocity contrasts can be another source of radial anisotropy (Backus, 1962). Compared to the upper and lowermost mantle, radial anisotropy in the MTZ has been less studied. Some early seismic tomography studies have highlighted that the MTZ is anisotropic (e.g., Beghein & Trampert, 2003; Montagner & Kennett, 1996; Visser et al., 2008), but others showed little or no anisotropy in this region (e.g., Beghein et al., 2006; Panning et al., 2010) or suggested that the observed radial anisotropy is not robust (e.g., Kustowski et al., 2008; Moulik & Ekström, 2014). More recently, there has been a renewed interest in mapping radial anisotropy in the whole mantle (see e.g., the review by Chang et al., 2014) and a number of studies even suggested the presence of azimuthal anisotropy in the MTZ (e.g., Schaeffer et al., 2016; Yuan & Beghein, 2013, 2014).

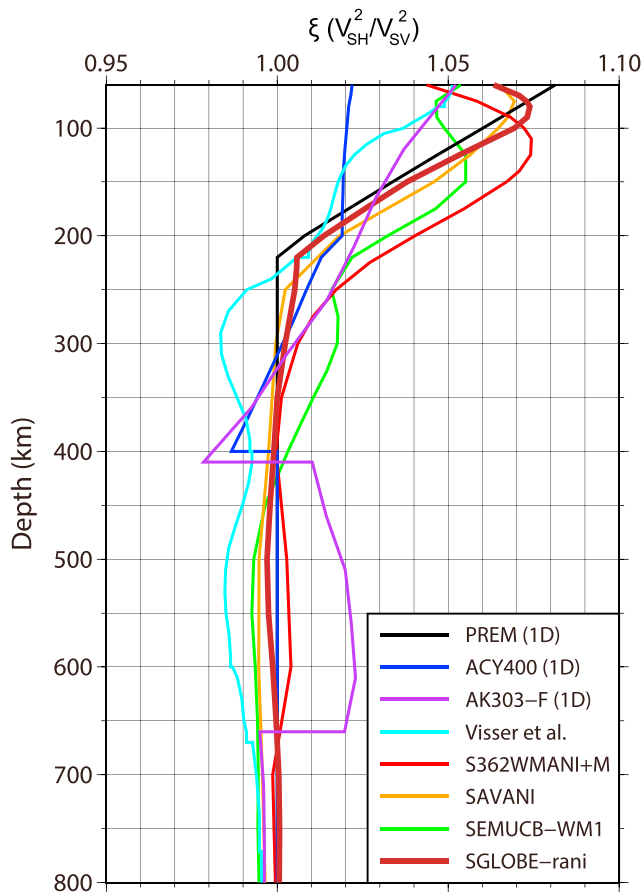


Figure 1. 1-D depth profiles from preliminary reference Earth model (PREM; Dziewoński & Anderson, 1981), ACY400 (Montagner & Anderson, 1989), and AK303-F (Montagner & Kennett, 1996) and average 1-D profiles from 3-D anisotropic models from Visser et al.'s (2008) model, S362WMANI+M (Moulik & Ekström, 2014), SAVANI (Auer et al., 2014), SEMUCB-WM1 (French & Romanowicz, 2014), and SGLOBE-rani (Chang et al., 2015).

In this study, we investigate the patterns of radial anisotropy in the MTZ in recent global tomography models, notably in the SGLOBE-rani model (Chang et al., 2015). Specifically, we focus on the MTZ beneath subduction zones in the western Pacific, since the data coverage is best for this region and strong anisotropy is likely to be observed there due to slab-induced strain (e.g., Faccenda, 2014a). We perform a series of robustness tests of the observed anisotropy features in the MTZ, which enables their physical interpretation in terms of LPO of the dominant minerals in the MTZ, notably wadsleyite. Furthermore, the water content of the MTZ is inferred from the strength of the observed radial anisotropy using experimental results from mineral physics on wadsleyite.

2. Radial Anisotropy in the Transition Zone

2.1. Tomographic Models

Several 1-D and 3-D global radial anisotropy models have been produced in the past 40 years (Figure 1). While there is good consistency between the large-scale isotropic features in different tomography models (e.g., Chang et al., 2015), global anisotropy images show substantial discrepancies. However, recent 3-D global models of radial anisotropy—S362WMANI+M (Moulik & Ekström, 2014), SAVANI (Auer et al., 2014), SEMUCB-WM1 (French & Romanowicz, 2014), and SGLOBE-rani (Chang et al., 2015)—consistently show weak global average anisotropy in the transition zone. Yet there are still considerable differences in the laterally varying anisotropic structure in the models (Figure 2). These discrepancies are likely due to differences in the data sets and in the modeling approaches employed (e.g., regularization and handling of crustal structure).

Nevertheless, most of the recent global models share a common feature of radial anisotropy in the MTZ: the presence of fast SV velocity anomalies near subduction zones. This feature was first reported by Panning and Romanowicz (2006) and has reappeared in other recent tomography models (Figure 2), except for the S362WMANI + M model. Figure 3a shows several contours of radial anisotropy anomalies in SGLOBE-rani near subduction zones in the western Pacific at 500-km depth (−1.0, −1.5, and −2.0% anomalies for orange, purple, and red contours, respectively).

Contour maps from other global anisotropy models are shown in Figure S1. Figure 3b shows a series of 1-D vertical profiles averaged over the −1.0% contoured areas in Figure 3a in solid lines for the global Earth models considered; for reference, the global 1-D averages of the models are also presented in dotted lines. Apart from S362WMANI+M, these profiles clearly show the presence of negative anisotropy (i.e., fast SV anomalies) in the transition zone, with the magnitude of the anisotropy being greatest at ~500-km depth and then decreasing as we reach the bottom of the transition zone. Remarkably, and as briefly pointed out by Chang et al. (2015), SGLOBE-rani shows narrow linear fast SV anomalies along subduction zones at 500-km depth in the western Pacific (Figure 2), which are comparable to the thickness of subducting slabs in the MTZ. Here we focus primarily on SGLOBE-rani rather than on other tomography models because we know the full details of its modeling procedure and because it shows a good association between fast SV anisotropy anomalies and subducted slabs in the MTZ.

Chang et al. (2015) give a detailed description of the construction of SGLOBE-rani, but, for completeness, here we briefly highlight its main features. First, a massive data set was used in its construction, including ~43,000,000 surface-wave dispersion measurements and ~420,000 body wave travel times. In particular, over 6,800,000 Rayleigh-wave and ~4,000,000 Love-wave overtone measurements up to sixth order were employed, which are strongly sensitive to the MTZ. Moreover, body wave travel times are also sensitive to anisotropy in the MTZ, and therefore, combining both data sets enhances the resolution of

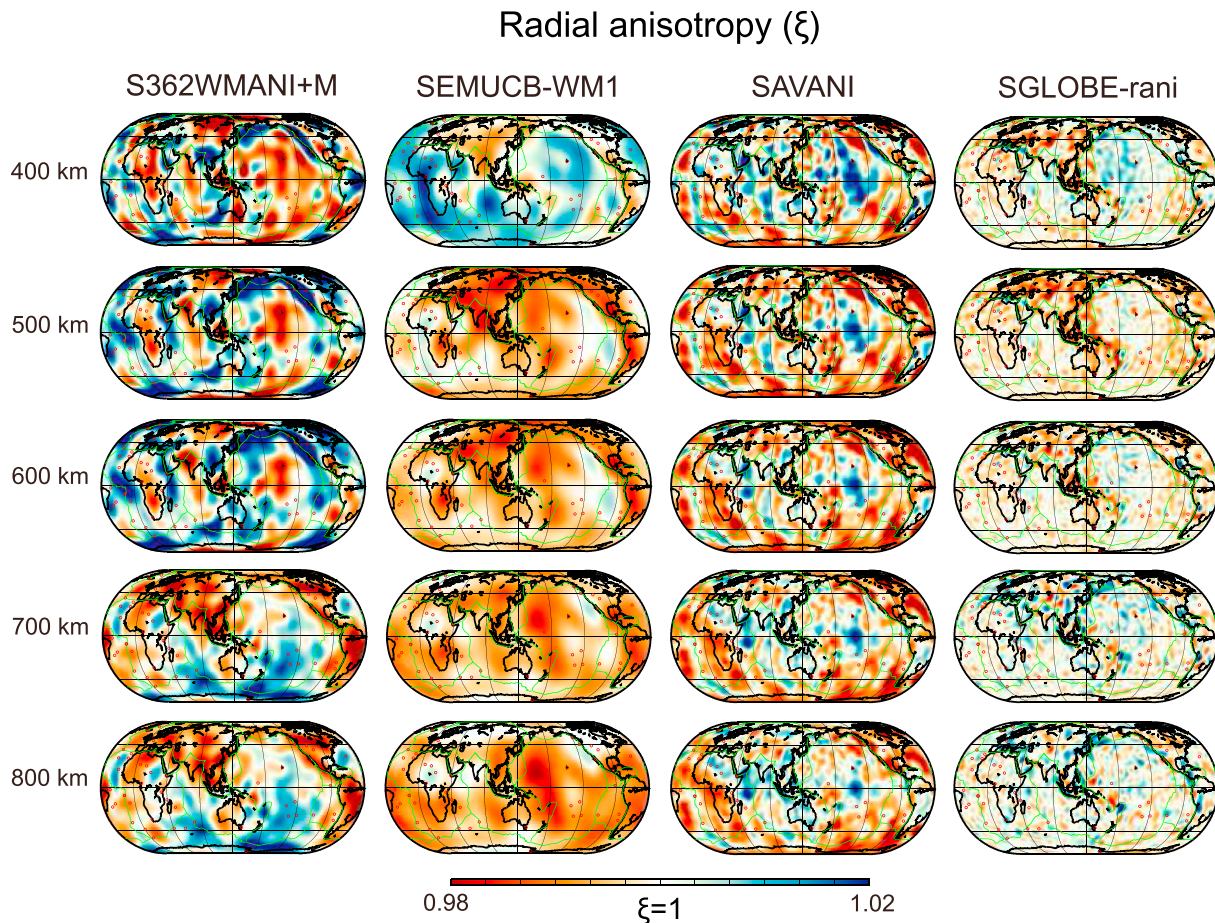


Figure 2. Depth slices of radial anisotropy ($\xi = \frac{V_{SH}^2}{V_{SV}^2}$) at 400-, 500-, 600-, 700-, and 800-km depth from S362WMANI+M (Moulik & Ekström, 2014), SEMUCB-WM1 (French & Romanowicz, 2014), SAVANI (Auer et al., 2014), and SGLOBE-rani (Chang et al., 2015).

anisotropy in the entire MTZ (Figure S2). Second, joint inversions of crustal and mantle structure were performed to better constrain mantle anisotropy, because crustal structure has a strong influence on the retrieved radial anisotropy in the mantle (e.g., Bozdağ & Trampert, 2008; Chang & Ferreira, 2017; Ferreira et al., 2010; Marone & Romanowicz, 2007; Panning et al., 2010). In particular, we utilized short-period fundamental-mode group-velocity data with a period range down to 16 s to constrain the crust. This is important, since Chang and Ferreira (2017) showed that short-period group-velocity data with a wave period down to at least 20 s are required to properly treat crustal effects in global radially anisotropic tomography.

2.2. Mineral Physics

Olivine, the dominant mineral in the upper mantle, transforms to wadsleyite at 410-km depth, which in turn transforms to ringwoodite at 520-km depth. Ringwoodite decomposes at 660-km depth into bridgmanite and ferropericlasite (e.g., Frost, 2008). If anisotropy in the transition zone is due to the alignment of intrinsically anisotropic mantle crystals by mantle flow, then the main source of the anisotropy must be wadsleyite, since other dominant mineral phases in this region (ringwoodite and majoritic garnet) are weakly anisotropic (e.g., Mainprice et al., 2000). Single-crystal V_S anisotropy of wadsleyite can reach ~9% at a pressure corresponding to 410-km depth (Zhang et al., 2018). Although such single-crystal V_S anisotropy may hinder the development of anisotropy above 1% globally in the MTZ, LPO may be produced (Thurel et al., 2003, 2003; Tommasi et al., 2004) in regions subjected to high strain, notably for shear strains much larger than 0.3 (e.g., Zhang et al., 2018). Wadsleyite is also reported to change its slip system with water content. Demouchy et al. (2011) first found a change of slip direction in wadsleyite at

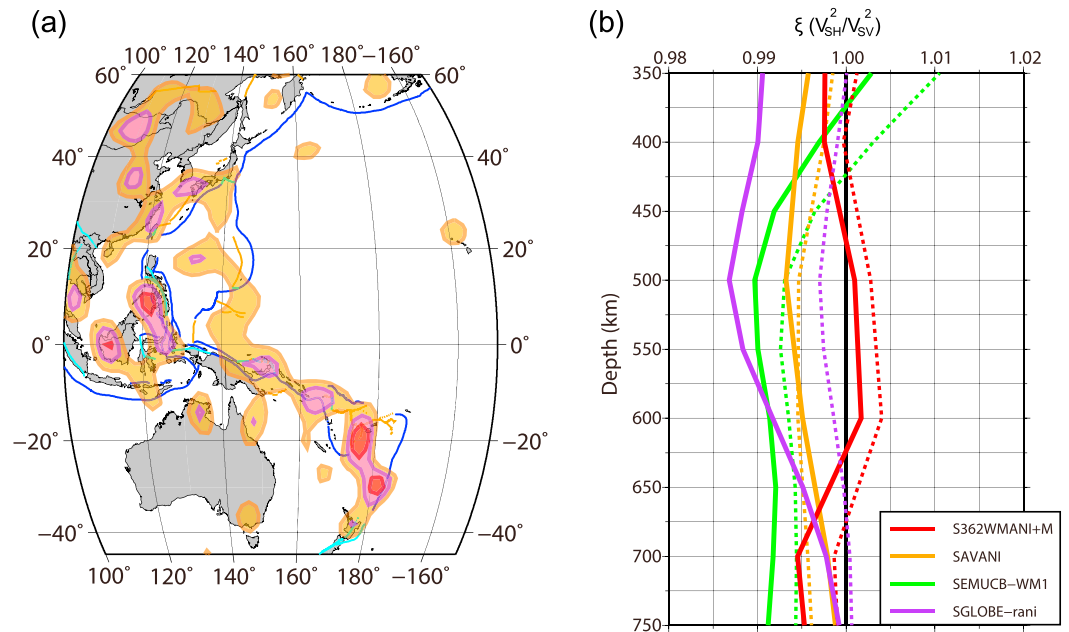


Figure 3. (a) The contours of -1.0 , -1.5 , and -2.0% perturbations in radial anisotropy at 500-km depth in SGLobe-rani are indicated by orange, purple, and red enclosed lines, respectively. (b) Comparison of the average 1-D profiles for the -1.0% contoured area (solid lines) in (a) and the whole mantle (dotted lines) in the 3-D global models S362WMANI+M (Moulik & Ekström, 2014), SAVANI (Auer et al., 2014), SEMUCB-WM1 (French & Romanowicz, 2014), and SGLobe-rani (Chang et al., 2015).

MTZ pressure and temperature from [100] to [001] when going from dry conditions to a water content of ~ 6000 ppm H/Si. Kawazoe et al. (2013) reported that the dominant slip system of wadsleyite is [001](010), if the water content is 1,000–3,700 ppm H/Si. Recently, Ohuchi et al. (2014) found that the dominant slip system of wadsleyite changes from [001](010) to [001](100) if the water content is over 9000 ppm H/Si (i.e., ~ 540 wt. ppm). A common feature in these different studies is that as the water content increases, the dominant slip system of wadsleyite seems to transform from [100](010) to [001](010) and then to [001](100). Nevertheless, the exact amount of water required for each of these transformations varies from study to study. Importantly, in all these slip systems, horizontal flow may cause negative radial anisotropy (i.e., faster SV velocity, $V_{SV} > V_{SH}$), whereas vertical flow may generate positive radial anisotropy (i.e., faster SH velocity). Ohuchi et al. (2014) also reported that the strength of radial anisotropy due to LPO development in wadsleyite aggregates decreases with water content over 3,000 ppm H/Si. Since the experiments of Ohuchi et al. use a wider range of hydrous conditions than in other mineral physics studies, in this study we use their results to interpret the seismological observations.

There are several other candidates for anisotropy in the MTZ than LPO of olivine polymorphs. Akimotoite, ilmenite-structured $MgSiO_3$, can be highly anisotropic (Li et al., 2009) at lower transition zone (LTZ) and uppermost lower mantle conditions. Zhang et al. (2005) reported that, generally, faster SV velocity is generated from akimotoite by vertical mantle flow, while faster SH velocity is generated by horizontal mantle flow. Some of the dense hydrous magnesium silicate (DHMS) phases can also be strongly anisotropic in the MTZ. Representative DHMS phases that are stable at MTZ conditions are phases B and D. Superhydrous phase B is less anisotropic than wadsleyite, whereas phase D can be more anisotropic than wadsleyite (Mookherjee & Tsuchiya, 2015). In case of horizontal mantle flow, phase D produces fast SH velocity (Rosa et al., 2012), similar to akimotoite. Thus, if anisotropy is present in the LTZ, it may be related to akimotoite, DHMS phase D, or SPO, since the dominant mineral in the lower part of the transition zone, ringwoodite, is weakly anisotropic. Nevertheless, these are minor phases with a limited thermal stability field (e.g., Frost, 1999; Pamato et al., 2015) and thus may not lead to large-scale anisotropy.

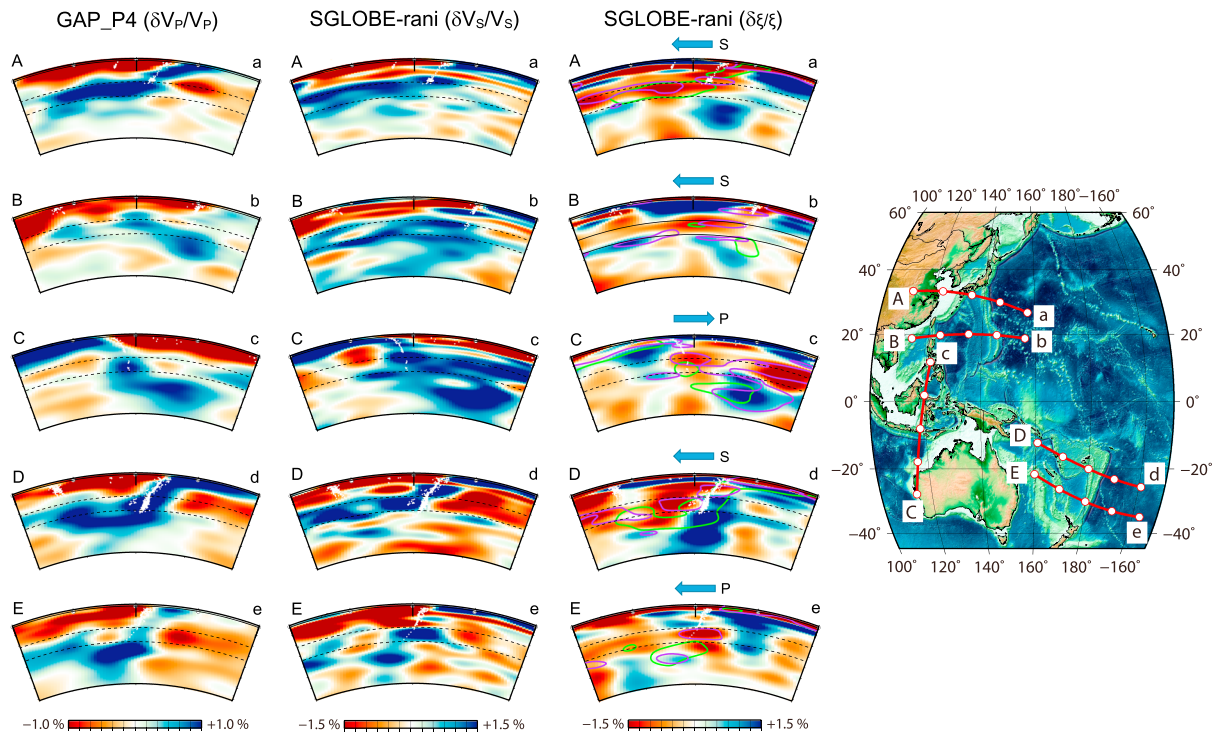


Figure 4. Cross sections across subduction zones in the western Pacific of P -velocity perturbations from GAP_P4 (Fukao & Obayashi, 2013) and perturbations of the Voigt average isotropy and radial anisotropy from SGLOBE-rani (Chang et al., 2015). V_P and V_S perturbations are measured from the average at each depth, but radial anisotropy is represented by perturbations from preliminary reference Earth model (Dziewoński & Anderson, 1981). The green and purple lines in the cross sections of radial anisotropy indicate contours of 0.8% of isotropic P -velocity perturbations from GAP_P4 and 1.3% of isotropic S -velocity perturbations from SGLOBE-rani, respectively, to match the locations of subducting slabs with patterns of radial anisotropy. The blue arrows and capital letters on top of radial anisotropy panels represent the direction and behavior (S, stagnating; P, penetrating) of subducting slabs, respectively.

3. Robustness of Radial Anisotropy in the MTZ Beneath the Western Pacific

Figure 4 presents five sets of cross sections of V_S and of radial anisotropy in SGLOBE-rani across subduction zones in the western Pacific. Additionally, we include V_P cross sections from the model GAP_P4 (Fukao & Obayashi, 2013), which is an isotropic model with good resolution near subducted slabs. For the five regions considered, we performed Backus-Gilbert resolution tests, which take into account the inversion's resolution matrix (Backus & Gilbert, 1968). Within these tests we compute Backus-Gilbert averaging kernels, which describe the spatial resolving power of our model. Ideally these kernels are delta functions in space. However, due to incomplete data coverage, regularization, and limitations in model parameterization, output kernels usually show a broad spatial extent. Figure S3 shows that SGLOBE-rani has very good vertical resolution for the isotropic structure in the MTZ beneath the western Pacific, showing *spike-like* Backus-Gilbert kernels. Regarding anisotropic structure, the kernels are broader, with a width of 600–1,700 km in the transition zone compared to 300–600 km for isotropic kernels in the same region. Nevertheless, they still show reasonable resolution in the upper transition zone (UTZ; 410–500 km), with the kernels clearly emerging from the zero line. They also show fair resolution even in the LTZ and in the uppermost lower mantle depth (600–700 km) beneath cross sections A-a, B-b, and D-d. As a caveat, one should bear in mind that the Backus-Gilbert resolution kernels do not give a complete picture of resolution; for example, they do not take into account limitations due to simplifications used in the forward modeling.

The cross sections show fast SH velocity anomalies in the uppermost mantle and in the top of the lower mantle beneath subducting slabs. In the MTZ, fast SV velocity anomalies are dominant along subducting slabs and tend to be stronger in the UTZ than in the LTZ in all cross sections of radial anisotropy except for the cross section D-d. Here a fast SH velocity anomaly is developed, likely due to the interaction between the Samoan mantle plume and the Tonga-Kermadec slabs (Chang et al., 2016). As shown in the third column

of Figure 4, there is a strong correlation between the morphology of fast SV velocity anomalies and the shape of the subducted slabs in the MTZ, which are marked by purple and green contours from the isotropic part of SGLOBE-rani and from GAP_P4, respectively. In order to check whether this correlation is caused by trade-offs between isotropic and anisotropic structure, we perform a synthetic resolution inversion test using only the isotropic part of SGLOBE-rani as the true input model (Figure S4). The exact same procedure and data coverage used to construct SGLOBE-rani is then utilized to invert for isotropic and anisotropic structure. We do not observe any strong leakage of isotropic structure into the retrieved anisotropy in the MTZ, which gives confidence that the observed anisotropic anomalies are not an artifact. We also test the possibility of leakage of anisotropic structure in the uppermost mantle to the MTZ (Figure S5). In this case, we use the whole isotropic part and the uppermost mantle anisotropic part of SGLOBE-rani down to 330 km as the true input model. The results show negligible leakage ($< 0.5\%$) of uppermost mantle anisotropy into the MTZ. Finally, we examine the trade-offs between anisotropy in the UTZ and in the LTZ by conducting the same test as in Figure S5, but now using as input model the anisotropic structure in SGLOBE-rani down to 590-km depth (Figure S6). Figure S6 shows only weak smearing at 600-km depth from anomalies at shallower depth.

For the slabs stagnant in the MTZ shown in cross sections A-a, B-b, and D-d, fast SV velocity anomalies seem to be elongated, whereas for the slabs penetrating into the lower mantle shown in cross sections C-c and E-e, we observe more localized anomalies near the slabs. As seen in the 1-D average profiles shown in Figure 3b, the strength of the fast SV velocity anomalies along subducted slabs tends to show maxima in the UTZ, decreasing abruptly in the LTZ. Thus, there is a clear depth dependency of radial anisotropy within the MTZ.

Comparing the amplitudes of the radial anisotropy anomalies in SGLOBE-rani with standard deviations from the probabilistic analysis of Beghein et al. (2006), anomalies of around -1.0% in the MTZ are over one standard deviation in their study. Therefore, anisotropy anomaly contours of -1.0 , -1.5 and -2.0% from SGLOBE-rani in Figure 3a may be beyond the error ranges. This supports the use of the amplitude information in SGLOBE-rani in comparisons with mineral physics experimental data, as performed in section 4.1 of this study.

In order to further quantitatively test the significance of the observed radial anisotropy anomalies in the MTZ, we performed statistical tests on SGLOBE-rani by comparing it to models obtained by inverting for isotropic and crustal thickness structure: (i) without allowing lateral variations in anisotropy (model A) and (ii) allowing lateral variations in anisotropy down to 330 km (model B). Specifically, we performed F tests by computing

$$F = \frac{[\chi^2(r) - \chi^2(p)] / (p - r)}{\chi^2(p) / (n - p)} \quad (1)$$

where χ^2 is the misfit function, n is the number of data points used in the inversions, and p , r are the numbers of model parameters for the two models which are under comparison ($p > r$). By calculating the integral probability $P_F(F; p - r, n - p)$ we can get the probability of how much the two models are different statistically (e.g., Bevington & Robinson, 2002). Since errors in the data and in the modeling employed in our inversions are essentially unknown, here we use the sum of the squares of the residuals (variance) as misfit function χ^2 (e.g., Forsyth, 1975). The variance reductions of SGLOBE-rani, model A, and model B are 0.763, 0.712, and 0.750, respectively. The probability that the improved fit of SGLOBE-rani compared to models A and B occurs by chance is less than 1%. Thus, the F tests support the significance of the radial anisotropy anomalies in the transition zone.

We also perform a cluster analysis of the radial anisotropy in the MTZ in SGLOBE-rani. Depth slices on a $2^\circ \times 2^\circ$ horizontal grid were assembled from 360- to 700-km depth, at an interval of 10 km. We then applied the MATLAB implementation of the K-means clustering algorithm (Lekic & Romanowicz, 2011; MacQueen, 1967) to the collection of depth slices. This technique divides the set of radial anisotropy profiles considered into K groups of similar profiles; in our study K varies from 2 to 4. An iterative approach is then followed, whereby the squared Euclidean distance metric is used to group the radial anisotropy profiles according to their similarity. Figure 5 shows the results obtained; different colors represent various regions identified (blue, red, brown, and orange). We find that the blue regions in

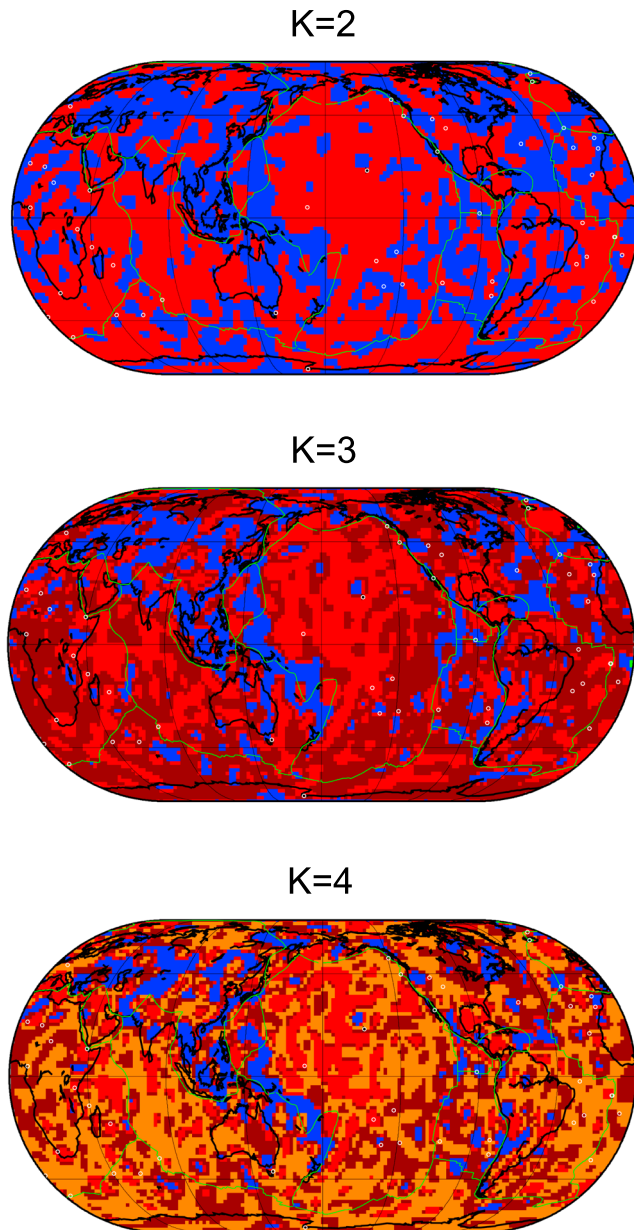


Figure 5. K-mean clustering tests for the distributions of radial anisotropy at 360- to 700-km depths with $K = 2, 3,$ and $4.$

hydrated layering), but the length-scale involved is likely much shorter than what can currently be resolved by global seismic tomography models.

4.1. Water Content in the MTZ

As explained previously, Ohuchi et al. (2014) found that the fabric strength of wadsleyite aggregates increases with decreasing water content. Figure 6 shows that if the water content is over 5,000 ppm H/Si, the radial anisotropy is weak ($\xi = V_{SV}^2/V_{SH}^2$ is mostly in the range 0.98–1 in open squares and circles) and does not seem to depend on water content (see the region highlighted in light orange in Figure 6). In contrast, if the water content is lower than 5,000 ppm H/Si (see the region highlighted in light blue in Figure 6), the anisotropy can reach values up to $\xi = 0.96$ (i.e., anomalies in radial anisotropy of -4% in open triangles). This is much larger than the observed radial anisotropy in the tomography models, which reaches at most $\sim -1.3\%$ in the UTZ in average (see Figure 3b and the purple shaded region in Figure 6).

each map clearly capture the radial anisotropy anomalies along subduction zones, particularly when $k = 3$ and $k = 4$. Thus, these anisotropy anomalies seem to comprise a statistically distinct group of anomalies within SGLOBE-rani. Intriguing anisotropy anomalies that are also captured within this group, such as beneath central Asia, may highlight past subduction events. However, the limited resolution of SGLOBE-rani in this region prevents further interpretations (Figure S2). Future work with additional seismic data is needed to investigate these features in detail.

4. The Origin of Radial Anisotropy in the MTZ: Water Content Implications

The observed pattern of negative radial anisotropy ($V_{SV} > V_{SH}$) in the transition zone, with a maximum at ~ 500 -km depth and weak values at the bottom of the MTZ, conforms well with results from mineral physics laboratory experiments. As mentioned in section 2.2, wadsleyite, a dominant mineral in the UTZ, is anisotropic, while ringwoodite and majoritic garnet, other dominant minerals in the MTZ, are nearly isotropic. Thus, the observed anisotropy is compatible with LPO of wadsleyite. This is further supported by 3-D numerical models of slab-induced deformation and associated mantle fabrics calculations, which yield values of radial anisotropy in the MTZ similar to the observations (Faccenda, 2014a). The weak negative anisotropy observed in the LTZ may be due to smearing effects from the seismic tomography inversions (Figure S6). It is unlikely that such negative anisotropy in the LTZ is due to akimotoite or DHMS phase D, since they would primarily generate faster SH velocity anomalies when subjected to horizontal strain by subducted slabs at the bottom of the transition zone (Zhang et al., 2005; Rosa et al., 2012; see section 2.2). On the other hand, SPO could potentially also contribute to the observed anisotropy, as suggested, for example, by Nowacki et al. (2015) as a possible explanation to source-side shear-wave splitting observations. However, recent calculations of radial anisotropy due to grain-scale SPO in a pyrolitic mantle using a mantle thermodynamics model suggest modest extrinsic anisotropy (SPO) throughout the mantle (Faccenda et al., 2019). Thus, our preferred mechanism of the observed anisotropy in the transition zone is LPO development in wadsleyite.

Nevertheless, we have to bear in mind that global tomography models such as SGLOBE-rani have low resolution of $\sim 1,000$ km and thus only illuminate large-scale Earth structure. Slabs in the LTZ may be possibly anisotropic due to akimotoite, DHMS phase D, and SPO (e.g., through

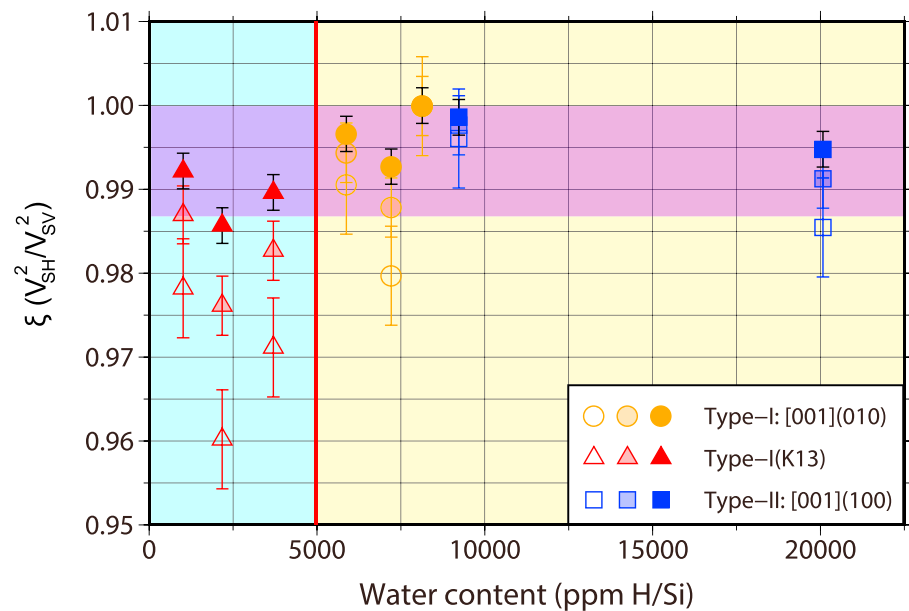


Figure 6. The strength of radial anisotropy in wadsleyite with respect to the water content in case of horizontal mantle flow using data from Ohuchi et al. (2014). Type-I and Type-II wadsleyite have dominant slip systems of [001](010) and [001](100), respectively. We also include data from Kawazoe et al. (2013) indicated by Type-I(K13). Open, translucent, and solid patterns indicate the strength of radial anisotropy of wadsleyite originally estimated by Ohuchi et al. (2014), with the dilution effect (wadsleyite: majoritic garnet = 60:40), and with the dilution and the damping effects in tomographic inversion, respectively. The purple shaded area indicates the range of radial anisotropy in the seismic profiles obtained for the -1.0% contoured area in Figure 3a. The uncertainties of open points are from the dependencies of V_{SH} and V_{SV} on the orientation of the wadsleyite samples.

However, if we take into account the dilution effect due to a pyrolytic mantle composition with 60% of wadsleyite and 40% volume of majoritic garnet (Irifune & Isshiki, 1998), assuming a linear relationship, the maximum predicted radial anisotropy anomaly in a UTZ with low water content decreases from -4% to -2.4% . In addition, one needs to bear in mind that the observed anisotropy in Figure 2 is lower than the actual mantle anisotropy due to the seismic tomography process, notably because of the regularization (damping) used to stabilize the tomographic inversions (e.g., Chang et al., 2014). We use synthetic inversion tests with SGLLOBE-rani as a true input model to estimate a damping effect of ~ 0.6 . In order to estimate this effect we average (i) the output anisotropic anomalies from the synthetic inversion within the -1.0% contoured area in Figure 3a and (ii) the anisotropic anomalies of SGLLOBE-rani in the same contour. A value of 0.6 is obtained from the ratio of the output and input anomalies. Applying this damping factor and a possible dilution effect to the results of Ohuchi et al. (2014), Figure 6 suggests that the expected radial anisotropy imaged by seismic tomography in a UTZ with low water content (3,000 ppm H/Si) may reach up to $\sim -1.5\%$ (solid triangles), which is compatible with at least some of the observations in Figures 2 and 3. Even though the anisotropy anomalies are small, we note that the contrast in radial anisotropy due to the water content varies up to a factor of two, which is not negligible. In particular, Figure 2 shows that there is a geographical variability in the strength of radial anisotropy in SGLLOBE-rani. For example, the MTZ beneath Tonga-Kermadec trenches, the Philippines, and the Sumatra trench show radial anisotropy anomalies that are stronger than -2.0% (Figure 3a). On the other hand, the Japan-Kuril-Kamchatka and Izu-Bonin-Mariana trenches seem to show weak radial anisotropy, with anomalies not exceeding -1% (Figure 3a). If we take the conservative approach of using radial anisotropy anomalies of -1.5% or stronger as a threshold for identifying regions with a water content lower than 3,000 ppm H/Si, this may imply that the UTZ beneath the Tonga-Kermadec trenches, the Philippines, and the Sumatra trench have a low water content. We also plotted contour maps for other anisotropy models in Figure S1. Although overall there are different patterns of anisotropy between the different models, it is interesting that S362WMANI+M, SEMUCB-WM1, and SAVANI commonly show strong negative anomalies beneath the Philippines and the Sumatra trench and SEMUCB-WM1 and SAVANI

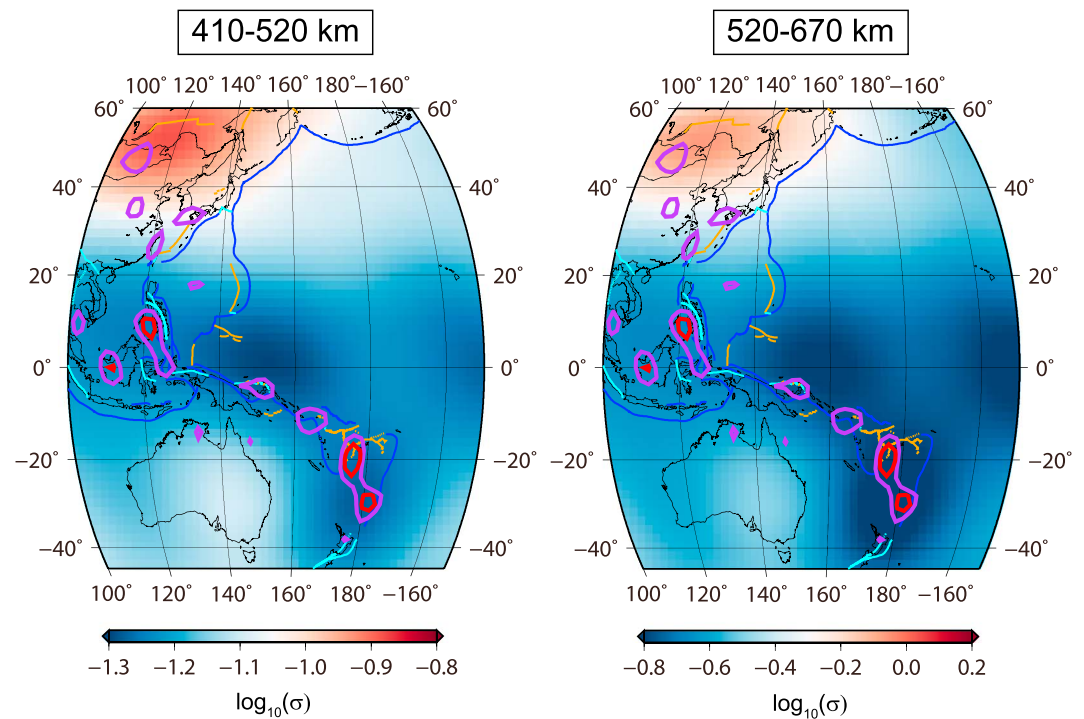


Figure 7. Mantle transition zone depth slices for electrical conductivity variations from Kelbert et al. (2009). The -1.5 and -2.0% contoured area of radial anisotropy at 500-km depth in SGLOBE-rani are indicated by purple and red enclosed lines, respectively. A symbol σ represents electrical conductivity.

indicate strong negative anomalies more than -1.5% beneath the Tonga-Kermadec trenches, as observed in SGLOBE-rani.

It is also noteworthy that relatively dry MTZ corresponds to regions where slabs penetrating into the lower mantle are observed (sections C-e and E-e in Figure 4). This may imply that the water content in the MTZ depends on the residence time of slabs in the MTZ (Faccenda, 2014b). Possibly not much water can be released to the MTZ by penetrating slabs due to their relatively short stay in the region. On the other hand, stagnant slabs may release more water due to their tendency to remain in the MTZ for a longer period of time.

4.2. Comparisons With Other Studies

Meier et al. (2009) performed a joint inversion of surface wave phase velocity data and topography of transition zone discontinuities to estimate the global distribution of water content in the MTZ. In their results, a dry MTZ is found beneath the Japan-Kuril-Kamchatka and the Sumatra regions, which is not consistent with our observations and with magnetotelluric studies (Ichiki et al., 2006; Koyama et al., 2006). Recently Thio et al. (2016) found that the topography of transition zone discontinuities currently cannot be used to constrain the water content in the MTZ due to large uncertainties on the mineral phase equilibria and a near-perfect trade-off between the water content and temperature increase.

In contrast, electrical conductivity is highly sensitive to hydrogen in minerals (Karato, 1990). Despite being also sensitive to iron content, the effect of water seems to be more significant (e.g., Yoshino & Katsura, 2009). Thus, electrical conductivity is a useful tool to constrain water in the mantle, even though the detailed water content of the MTZ based on conductivity studies is still debated (e.g., Karato, 2011). Kelbert et al. (2009) built a 3-D global model of electrical conductivity variations by inverting long period geomagnetic response functions. Intriguingly, our results match well this global electrical conductivity model, when interpreted in terms of variations of water content in the MTZ (Figure 7). In particular, Kelbert et al.'s model shows relatively low electrical conductivity in the Tonga-Kermadec trenches, the Philippines, and the Sumatra trench at 410- to 670-km depth. This is compatible with a low water content, whereas the Japan-Kuril-Kamchatka

and the Izu-Bonin-Mariana regions show higher conductivity, and thus are likely wetter. The consistency between our results and these totally independent studies is encouraging. It may add confidence that the dependency of fabric strength of wadsleyite on water content and the associated radial anisotropy can be used as a proxy to map the water content in the MTZ.

Although a number of studies have suggested a water-rich MTZ, from investigations of observed ringwoodite diamond inclusions (Pearson et al., 2014) to regional seismological analyses of reflected phases (e.g., Schmandt et al., 2014), electrical conductivity models (e.g., Karato, 2011), and laboratory measurements of mineral viscosity (Fei et al., 2017), our study suggests a regional variability in possible water content even beneath subduction zones that is more complex than previously thought.

5. Discussion and Conclusions

Similar to some other recent radially anisotropic models (e.g., Auer et al., 2014; French & Romanowicz, 2014), SGLOBE-rani shows strong fast *SV* anomalies in the UTZ beneath subduction zones in the western Pacific. In addition, source-side anisotropy studies also show localized anisotropy near subducted slabs in the transition zone (e.g., Foley & Long, 2011; Mohiuddin et al., 2015; Nowacki et al., 2015). SGLOBE-rani's fast *SV* anomalies in the UTZ decrease with depth, which is consistent with LPO development in wadsleyite. Using an inversely proportional relationship between radial anisotropy and water content predicted from deformation experiments on wadsleyite aggregates (Ohuchi et al., 2014), we might get inferences on the water content in the MTZ beneath subduction zones. We suggest that the MTZ beneath the Tonga-Kermadec trenches, the Philippines, and the Sumatra trench may be relatively dry (water content smaller than 3,000 ppm H/Si).

These conclusions are subject to the caveat that there are likely uncertainties in the estimates of (i) the dilution effect, due to the assumption of a simple pyrolitic composition; (ii) the relationship between water content and radial anisotropy from the mineral physics experiments by Ohuchi et al., as future repeated experiments will be needed for proper error quantification; (iii) the tomographic damping effect, which may vary spatially; and (iv) the impact of the theoretical approximations used to build the tomographic models. Both amplitude information from tomography and mineral physics experiments may not be well constrained.

Recently, Cline II et al. (2018) suggested that wave speeds and attenuation are insensitive to water content in the upper mantle based on experiments with Ti-doped olivine. Moreover, Buchen et al. (2018) performed high-pressure sound wave speed and density measurements of wadsleyite to conclude that impedance contrast across the 410-km discontinuity is a more robust indicator of water in the transition zone than wave speed variations. However, Buchen et al.'s study involved extrapolations to realistic mantle temperatures and did not consider LPO in the measurements, while Cline II et al.'s experiments were performed at conditions of lower pressure (0.2 GPa) than actual mantle pressures. Moreover, the mobility of artificial crystal defects (i.e., defects introduced by Ti) might be different from the defects intrinsic to natural olivine (Irifune & Ohuchi, 2018). Hansen et al. (2016) reported that the strength of radial anisotropy in olivine aggregates under simple shear is inversely proportional to the water content, which is similar to the reports by Ohuchi et al. regarding wadsleyite. In addition, recently Zhang et al. (2018) carried out high-pressure experiments on wadsleyite and also found a decrease in single-crystal anisotropy as water content increases. Although they do not report values of radial anisotropy versus water content that can be readily used in interpretations of radially anisotropic tomography, the trend found in their study is overall compatible with the data of Ohuchi et al. (2014), which are used in this study. Zhang et al. (2018) report that it is difficult to develop LPO globally in a moderately hydrated transition zone, apart from in regions of high strain (for shear strain larger than 0.3). The findings of Zhang et al. (2018) are therefore consistent with recent models of radial anisotropy are on average isotropic in the MTZ (Figure 3) and with our observations that radial anisotropy anomalies of $\sim 1.5\%$ are mostly confined around subduction zones, where shear strains may be on average ~ 2 (e.g., Faccenda, 2014a). Our findings also agree remarkably well with an independent global model of electrical conductivity (Kelbert et al., 2009), which may suggest that despite possible errors affecting our results, the relationship between radial anisotropy and water content may dominate over other factors. We hope that our interpretation will stimulate further seismological and mineral physics studies on the origin of anisotropy within the transition zone.

Acknowledgments

We thank Tomohiro Ohuchi and Anna Kelbert for fruitful discussions and for providing us their data. The mineral physics experimental data are available at <http://seismo.kangwon.ac.kr/downloads.html>. Tomographic models used in this paper are available from IRIS Data Services Products (<http://ds.iris.edu/ds/products/emc-earthmodels/>). This research was supported by the Korea Meteorological Administration Research and Development Program under grant KMI2018-09312. A. M. G. F. thanks support from NERC grant NE/N011791/1. We are very grateful for the thorough proof-reading by Martha Pamato, notably of the mineral physics part of the manuscript. We also thank Andy Thomson, Simon Hunt, and David Dobson for fruitful discussions.

References

- Auer, L., Boschi, L., Becker, T. W., Nissen-Meyer, T., & Giardini, D. (2014). Savani: A variable resolution whole-mantle model of anisotropic shear velocity variations based on multiple data sets. *Journal of Geophysical Research: Solid Earth*, *119*, 3006–3034. <https://doi.org/10.1002/2013JB010773>
- Backus, G. E. (1962). Long-wave elastic anisotropy produced by horizontal layering. *Journal of Geophysical Research*, *67*(11), 4427–4440. <https://doi.org/10.1029/JZ067i011p04427>
- Backus, G. E., & Gilbert, J. F. (1968). The resolving power of gross Earth data. *Geophysical Journal of the Royal Astronomical Society*, *16*(2), 169–205. <https://doi.org/10.1111/j.1365-246X.1968.tb00216.x>
- Beghein, C., & Trampert, J. (2003). Probability density functions for radial anisotropy: Implications for the upper 1200 km of the mantle. *Earth and Planetary Science Letters*, *217*, 151–162.
- Beghein, C., Trampert, J., & van Heijst, H. J. (2006). Radial anisotropy in seismic reference models of the mantle. *Journal of Geophysical Research*, *111*, B02303. <https://doi.org/10.1029/2005JB003728>
- Bercovici, D., & Karato, S.-I. (2003). Whole-mantle convection and the transition-zone water filter. *Nature*, *425*(6953), 39–44. <https://doi.org/10.1038/nature01918>
- Bevington, P. R., & Robinson, D. K. (2002). *Data reduction and error analysis for the physical sciences* (3rd ed.). New York: McGraw-Hill.
- Bozdağ, E., & Trampert, J. (2008). On crustal corrections in surface wave tomography. *Geophysical Journal International*, *172*(3), 1066–1082. <https://doi.org/10.1111/j.1365-246X.2007.03690.x>
- Buchen, J., Marquardt, H., Speziale, S., Kawazoe, T., Ballaran, T. B., & Kurmosov, A. (2018). High-pressure single-crystal elasticity of wadsleyite and the seismic signature of water in the shallow transition zone. *Earth and Planetary Science Letters*, *498*, 77–87.
- Chang, S.-J., & Ferreira, A. M. G. (2017). Improving global radial anisotropy tomography: The importance of simultaneously inverting for crustal and mantle structure. *Bulletin of the Seismological Society of America*, *107*(2), 624–638. <https://doi.org/10.1785/0120160142>
- Chang, S.-J., Ferreira, A. M. G., & Faccenda, M. (2016). Upper- and mid-mantle interaction between the Samoan plume and the Tonga-Kermadec slabs. *Nature Communications*, *7*(1), 10799. <https://doi.org/10.1038/ncomms10799>
- Chang, S.-J., Ferreira, A. M. G., Ritsema, J., van Heijst, H. J., & Woodhouse, J. H. (2014). Global radially anisotropic mantle structure from multiple datasets: A review, current challenges, and outlook. *Tectonophysics*, *617*, 1–19. <https://doi.org/10.1016/j.tecto.2014.01.033>
- Chang, S.-J., Ferreira, A. M. G., Ritsema, J., van Heijst, H. J., & Woodhouse, J. H. (2015). Joint inversion for global isotropic and radially anisotropic mantle structure including crustal thickness perturbations. *Journal of Geophysical Research: Solid Earth*, *120*, 4278–4300. <https://doi.org/10.1002/2014JB011824>
- Cline II, C. J., Faul, U. H., David, E. C., Berry, A. J., & Jackson, I. (2018). Redox-influenced seismic properties of upper-mantle olivine. *Nature*, *555*(7696), 355–358. <https://doi.org/10.1038/nature25764>
- Demouchy, S., Mainprice, D., Tommasi, A., Couvy, H., Barou, F., Frost, D. J., & Cordier, P. (2011). Forsterite to wadsleyite phase transformation under shear stress and consequences for the Earth's mantle transition zone. *Physics of the Earth and Planetary Interiors*, *184*(1–2), 91–104. <https://doi.org/10.1016/j.pepi.2010.11.001>
- Dziewoński, A. M., & Anderson, D. L. (1981). Preliminary reference Earth model. *Physics of the Earth and Planetary Interiors*, *25*(4), 297–356. [https://doi.org/10.1016/0031-9201\(81\)90046-7](https://doi.org/10.1016/0031-9201(81)90046-7)
- Faccenda, M. (2014a). Mid mantle seismic anisotropy around subduction zones. *Physics of the Earth and Planetary Interiors*, *227*, 1–19. <https://doi.org/10.1016/j.pepi.2013.11.015>
- Faccenda, M. (2014b). Water in the slab: A trilogy. *Tectonophysics*, *614*, 1–30. <https://doi.org/10.1016/j.tecto.2013.12.020>
- Faccenda, M., Ferreira, A. M. G., Tisato, N., Lithgow-Bertelloni, C. R., Stixrude, L. P., & Pennacchioni, G. (2019). Extrinsic elastic anisotropy in a compositionally heterogeneous Earth's mantle. *Journal of Geophysical Research: Solid Earth*, *124*. <https://doi.org/10.1029/2018JB016482>
- Fei, H., Yamazaki, D., Sakurai, M., Miyajima, N., Ohfuji, H., Katsura, T., & Yamamoto, T. (2017). A nearly water-saturated mantle transition zone inferred from mineral viscosity. *Science Advances*, *3*(6), e1603024. <https://doi.org/10.1126/sciadv.1603024>
- Ferreira, A. M. G., Woodhouse, J. H., Visser, K., & Trampert, J. (2010). On the robustness of global radially anisotropic surface wave tomography. *Journal of Geophysical Research*, *115*, B04313. <https://doi.org/10.1029/2009JB006716>
- Foley, B., & Long, M. D. (2011). Upper and mid-mantle anisotropy beneath the Tonga slab. *Geophysical Research Letters*, *38*, L02303. <https://doi.org/10.1029/2010GL046021>
- Forsyth, D. W. (1975). The early structural evolution and anisotropy of the oceanic upper mantle. *Geophysical Journal of the Royal Astronomical Society*, *43*(1), 103–162. <https://doi.org/10.1111/j.1365-246X.1975.tb00630.x>
- French, S. W., & Romanowicz, B. (2014). Whole-mantle radially anisotropic shear velocity structure from spectral-element waveform tomography. *Geophysical Journal International*, *199*, 1303–1327. <https://doi.org/10.1093/gji/ggu334>
- Frost, D. J. (1999). The stability of dense hydrous magnesium silicates in Earth's transition zone and lower mantle. In Y. Fei, C. M. Bertka, & B. O. Mysen (Eds.), *Mantle petrology: Field observations and high pressure experimentation: A tribute to Francis (Joe) Boyd, the Geochemical Society Special Publication* (Vol. 6, pp. 283–296). Houston: The Geochemical Society.
- Frost, D. J. (2008). The upper mantle and transition zone. *Elements*, *4*(3), 171–176. <https://doi.org/10.2113/GSELEMENTS.4.3.171>
- Fukao, Y., & Obayashi, M. (2013). Subducted slabs stagnant above, penetrating through, and trapped below the 660 km discontinuity. *Journal of Geophysical Research: Solid Earth*, *118*, 5920–5938. <https://doi.org/10.1002/2013JB010466>
- Hansen, L. N., Qi, C., & Warren, J. M. (2016). Olivine anisotropy suggests Gutenberg discontinuity is not the base of the lithosphere. *Proceedings of the National Academy of Sciences of the United States of America*, *113*(38), 10,503–10,506. <https://doi.org/10.1073/pnas.1608269113>
- Hirschmann, M. M. (2006). Water, melting, and the deep Earth H₂O cycle. *Annual Review of Earth and Planetary Sciences*, *34*(1), 629–653. <https://doi.org/10.1146/annurev.earth.34.031405.125211>
- Ichiki, M., Baba, K., Obayashi, M., & Utada, H. (2006). Water content and geotherm in the upper mantle above stagnant slab: Interpretation of electrical conductivity and seismic P-wave velocity models. *Physics of the Earth and Planetary Interiors*, *155*(1–2), 1–15. <https://doi.org/10.1016/j.pepi.2005.09.010>
- Irfune, T., & Isshiki, M. (1998). Iron partitioning in a pyrolite mantle and the nature of the 410-km seismic discontinuity. *Nature*, *392*(6677), 702–705. <https://doi.org/10.1038/33663>
- Irfune, T., & Ohuchi, T. (2018). Oxidation softens mantle rocks. *Nature News & Views*, *555*(7696), 314–315. <https://doi.org/10.1038/d41586-018-02828-y>
- Karato, S. (1990). The role of hydrogen in the electrical conductivity of the upper mantle. *Nature*, *347*(6290), 272–273. <https://doi.org/10.1038/347272a0>

- Karato, S. (2011). Water distribution across the mantle transition zone and its implications for global material circulation. *Earth and Planetary Science Letters*, 301(3-4), 413–423. <https://doi.org/10.1016/j.epsl.2010.11.038>
- Kawazoe, T., Ohuchi, T., Nishihara, Y., Nishiyama, N., Fujino, K., & Irifune, T. (2013). Seismic anisotropy in the mantle transition zone induced by shear deformation of wadsleyite. *Physics of the Earth and Planetary Interiors*, 216, 91–98. <https://doi.org/10.1016/j.pepi.2012.12.005>
- Kelbert, A., Schultz, A., & Egbert, G. (2009). Global electromagnetic induction constraints on transition-zone water content variations. *Nature*, 460(7258), 1003–1006. <https://doi.org/10.1038/nature08257>
- Kohlstedt, D. L., Keppeler, H., & Rubie, D. C. (1996). The solubility of water in α , β and γ phases of $(\text{Mg,Fe})_2\text{SiO}_4$. *Contributions to Mineralogy and Petrology*, 123(4), 345–357. <https://doi.org/10.1007/s004100050161>
- Koyama, T., Shimizu, H., Utada, H., Ichiki, M., Ohtani, E., & Hae, R. (2006). Water content in the mantle transition zone beneath the North Pacific derived from the electrical conductivity anomaly. In S. D. Jacobsen & S. van der Lee (Eds.), *Earth's Deep Water Cycle, Geophysical Monograph* (Vol. 168, pp. 171–179). Washington, DC: American Geophysical Union.
- Kustowski, B., Ekström, G., & Dziewonski, A. M. (2008). Anisotropic shear-wave velocity structure of the Earth's mantle: A global model. *Journal of Geophysical Research*, 113, B06306. <https://doi.org/10.1029/2007JB005169>
- Lekic, V., & Romanowicz, B. (2011). Tectonic regionalization without a priori information: A cluster analysis of upper mantle tomography. *Earth and Planetary Science Letters*, 308(1-2), 151–160. <https://doi.org/10.1016/j.epsl.2011.05.050>
- Li, L., Weidner, D. J., Brodholt, J., Alfe, D., & Price, G. D. (2009). *Ab initio* molecular dynamics study of elasticity of akimotoite MgSiO_3 at mantle conditions. *Physics of the Earth and Planetary Interiors*, 173(1-2), 115–120. <https://doi.org/10.1016/j.pepi.2008.11.005>
- MacQueen, J. (1967). Some methods for classification and analysis of multivariate observations. In L. M. le Cam & J. Neyman (Eds.), *Proceedings of the Fifth Berkeley Symposium on Mathematical Statistics and Probability* (Vol. 1, pp. 281–297). Berkeley: University of California Press.
- Mainprice, D., Barruol, G., & Ben Ismail, W. (2000). The seismic anisotropy of the Earth's mantle: From single crystal to polycrystal. In S.-I. Karato, A. M. Forte, R. C. Liebermann, G. Masters, & L. Stixrude (Eds.), *Earth's Interior: Mineral physics and tomography from the atomic to the global scale, Geophysical Monograph* (Vol. 117, pp. 237–264). Washington, DC: American Geophysical Union. <https://doi.org/10.1029/GM117p0237>
- Marone, F., & Romanowicz, B. (2007). Non-linear crustal corrections in high-resolution regional waveform seismic tomography. *Geophysical Journal International*, 170(1), 460–467. <https://doi.org/10.1111/j.1365-246X.2007.03399.x>
- Meier, U., Trampert, J., & Curtis, A. (2009). Global variations of temperature and water content in the mantle transition zone from higher mode surface waves. *Earth and Planetary Science Letters*, 282(1-4), 91–101. <https://doi.org/10.1016/j.epsl.2009.03.004>
- Mohiuddin, A., Long, M. D., & Lynner, C. (2015). Mid-mantle seismic anisotropy beneath southwestern Pacific subduction systems and implications for mid-mantle deformation. *Physics of the Earth and Planetary Interiors*, 245, 1–14. <https://doi.org/10.1016/j.pepi.2015.05.003>
- Montagner, J.-P. (1998). Where can seismic anisotropy be detected in the Earth's model? In boundary layers *Pure and Applied Geophysics*, 151(4), 223–256. <https://doi.org/10.1007/s000240050113>
- Montagner, J.-P., & Anderson, D. L. (1989). Constrained reference mantle model. *Physics of Earth and Planetary Interiors*, 58(2-3), 205–227. [https://doi.org/10.1016/0031-9201\(89\)90055-1](https://doi.org/10.1016/0031-9201(89)90055-1)
- Montagner, J.-P., & Kennett, B. L. N. (1996). How to reconcile body-wave and normal-mode reference Earth models. *Geophysical Journal International*, 125(1), 229–248. <https://doi.org/10.1111/j.1365-246X.1996.tb06548.x>
- Mookherjee, M., & Tsuchiya, J. (2015). Elasticity of superhydrous phase, $\text{B, Mg}_{10}\text{Si}_3\text{O}_{14}(\text{OH})_4$. *Physics of the Earth and Planetary Interiors*, 238, 42–50. <https://doi.org/10.1016/j.pepi.2014.10.010>
- Moulik, P., & Ekström, G. (2014). An anisotropic shear velocity model of the Earth's mantle using normal modes, body waves, surface waves and long-period waveforms. *Geophysical Journal International*, 199(3), 1713–1738. <https://doi.org/10.1093/gji/ggu356>
- Nowacki, A., Kendall, J.-M., Wookey, J., & Pemberton, A. (2015). Mid-mantle anisotropy in subduction zones and deep water transport. *Geochemistry, Geophysics, Geosystems*, 16, 764–784. <https://doi.org/10.1002/2014GC005667>
- Nowacki, A., Wookey, J., & Kendall, J.-M. (2011). New advances in using seismic anisotropy, mineral physics and geodynamics to understand deformation in the lowermost mantle. *Journal of Geodynamics*, 52(3-4), 205–228. <https://doi.org/10.1016/j.jog.2011.04.003>
- Ohuchi, T., Fujino, K., Kawazoe, T., & Irifune, T. (2014). Crystallographic preferred orientation of wadsleyite and ringwoodite: Effects of phase transformation and water on seismic anisotropy in the mantle transition zone. *Earth and Planetary Science Letters*, 397, 133–144. <https://doi.org/10.1016/j.epsl.2014.03.066>
- Pamato, M. G., Myhill, R., Ballaran, T. B., Frost, D. J., Heidebach, F., & Miyajima, N. (2015). Lower-mantle water reservoir implied by the extreme stability of a hydrous aluminosilicate. *Nature Geoscience*, 8(1), 75–79. <https://doi.org/10.1038/ngeo2306>
- Panning, M. P., Lekic, V., & Romanowicz, B. (2010). Importance of crustal corrections in the development of a new global model of radial anisotropy. *Journal of Geophysical Research*, 115, B12325. <https://doi.org/10.1029/2010JB007520>
- Panning, M. P., & Romanowicz, B. (2006). A three-dimensional radially anisotropic model of shear velocity in the whole mantle. *Geophysical Journal International*, 167(1), 361–379. <https://doi.org/10.1111/j.1365-246X.2006.03100.x>
- Pearson, D. G., Brenker, F. E., Nestola, F., McNeill, J., Nasdala, L., Huchison, M. T., et al. (2014). Hydrous mantle transition zone indicated by ringwoodite included within diamond. *Nature*, 507, 221–224.
- Rosa, A. D., Sanchez-Valle, C., & Ghosh, S. (2012). Elasticity of phase D and implication for the degree of hydration of deep subducted slabs. *Geophysical Research Letters*, 39, L06304. <https://doi.org/10.1029/2012GL050927>
- Schaeffer, A. J., Lebedev, S., & Becker, T. W. (2016). Azimuthal seismic anisotropy in the Earth's upper mantle and the thickness of tectonic plates. *Geophysical Journal International*, 207(2), 901–933. <https://doi.org/10.1093/gji/ggw309>
- Schmandt, B., Jacobsen, S. D., Becker, T. W., Liu, Z., & Dueker, K. G. (2014). Dehydration melting at the top of the lower mantle. *Science*, 344(6189), 1265–1268. <https://doi.org/10.1126/science.1253358>
- Silver, P. G. (1996). Seismic anisotropy beneath the continents: Probing the depths of geology. *Annual Review of Earth and Planetary Sciences*, 24(1), 385–432. <https://doi.org/10.1146/annurev.earth.24.1.385>
- Smyth, J. R. (1987). $\beta\text{-Mg}_2\text{SiO}_4$: A potential host for water in the mantle? *American Mineralogist*, 72, 1051–1055.
- Thio, V., Cobden, L., & Trampert, J. (2016). Seismic signature of a hydrous mantle transition zone. *Physics of the Earth and Planetary Interiors*, 250, 46–63. <https://doi.org/10.1016/j.pepi.2015.11.005>
- Thurel, E., Cordier, P., Frost, D. J., & Karato, S.-I. (2003). Plastic deformation of wadsleyite: II. High-pressure deformation in shear. *Physics and Chemistry of Minerals*, 30, 267–270.
- Thurel, E., Douin, J., & Cordier, P. (2003). Plastic deformation of wadsleyite: III. Interpretation of dislocations and slip systems. *Physics and Chemistry of Minerals*, 30, 271–279.

- Tommasi, A., Mainprice, D., Cordier, P., Thoraval, C., & Couvy, H. (2004). Strain-induced seismic anisotropy of wadsleyite polycrystals and flow patterns in the mantle transition zone. *Journal of Geophysical Research*, *109*, B12405. <https://doi.org/10.1029/2004JB003158>
- Visser, K., Trampert, J., Lebedev, S., & Kennett, B. L. N. (2008). Probability of radial anisotropy in the deep mantle. *Earth and Planetary Science Letters*, *270*(3-4), 241–250. <https://doi.org/10.1016/j.epsl.2008.03.041>
- Yoshino, T., & Katsura, T. (2009). Effect of iron content on electrical conductivity of ringwoodite, with implications for electrical structure in the transition zone. *Physics of the Earth and Planetary Interiors*, *174*(1-4), 3–9. <https://doi.org/10.1016/j.pepi.2008.09.015>
- Yuan, K., & Beghein, C. (2013). Seismic anisotropy changes across upper mantle phase transitions. *Earth and Planetary Science Letters*, *374*, 132–144. <https://doi.org/10.1016/j.epsl.2013.05.031>
- Yuan, K., & Beghein, C. (2014). Three-dimensional variations in Love and Rayleigh wave azimuthal anisotropy for the upper 800 km of the mantle. *Journal of Geophysical Research: Solid Earth*, *119*, 3232–3255. <https://doi.org/10.1002/2013JB010853>
- Zhang, J. S., Bass, J. D., & Schmandt, B. (2018). The elastic anisotropy change near the 410-km discontinuity: Predictions from single-crystal elasticity measurements of olivine and wadsleyite. *Journal of Geophysical Research: Solid Earth*, *123*, 2674–2684. <https://doi.org/10.1002/2017JB015339>
- Zhang, Y., Zhao, D., & Matsui, M. (2005). Anisotropy of akimotoite: A molecular dynamics study. *Physics of the Earth and Planetary Interiors*, *151*(3-4), 309–319. <https://doi.org/10.1016/j.pepi.2005.04.003>